HHS Public Access

Author manuscript

IEEE Trans Ultrason Ferroelectr Freq Control. Author manuscript; available in PMC 2018 May 01.

Published in final edited form as:

IEEE Trans Ultrason Ferroelectr Freq Control. 2017 May ; 64(5): 798–810. doi:10.1109/TUFFC.2017.2681695.

Targeting Effects on the Volume of the Focused Ultrasound Induced Blood-Brain Barrier Opening in Non-Human Primates *in vivo*

Maria Eleni Karakatsani,
Department of Biomedical Engineering, Columbia University, New York, NY 10025 USA

Gesthimani Samiotaki,
Department of Biomedical Engineering, Columbia University, New York, NY 10025 USA

Matthew E. Downs,
Department of Biomedical Engineering, Columbia University, New York, NY 10025 USA

Vincent P. Ferrera, and
Department of Neuroscience, Columbia University, New York, NY 10032 USA

Elisa E. Konofagou
Departments of Biomedical Engineering and Radiology, Columbia University, New York, NY 10025 USA

Abstract

Drug delivery to subcortical regions is susceptible to the blood-brain barrier (BBB) impeding the molecular exchange between the blood stream and the brain parenchyma. Focused ultrasound coupled with the administration of microbubbles has been proven to open the BBB locally, transiently and non-invasively both in rodents and in Non-Human-Primates (NHPs). The development of this disruption technique independent of MRI monitoring is of primordial importance yet restrained to the targeting optimization. The current paper establishes the linear relationship of the incidence angle with the volume of BBB opening (V_{BBB}) and the Peak Negative Pressure (PNP) when sonicating the Caudate Nucleus and the Putamen region of five non-human-primates. In addition, the effect of central nervous system structures on the opening morphology is evaluated by identification of the gray-to-white-matter ratio at the opening site. Finally, the targeting accuracy is assessed through estimation of the geometric and angle shift of the opening from the targeted region. Interestingly, results prove a monotonic increase of the opening volume with close to normal incidence angles. Moreover, 80.35% of the opening lies on gray matter regions compared to only 19.41% attributed to the white matter. The opening was found to be shifted axially, towards the transducer, and laterally with an average angle shift at 4.5°. Finally, we were capable of showing reproducibility of targeting accuracy with the same stereotactic and ultrasonic parameters. This study documents the *a priori* prediction of the opening volume through manipulation of the angle and pressure as well as establishing the predictability, accuracy and safety of FUS induced BBB opening in NHPs.

DISCLOSURE/CONFLICT OF INTEREST
The authors declare no conflict of interest.

Index Terms

focused-ultrasound; blood-brain barrier; incidence angle; geometric shift; gray matter; white matter

I. Introduction

The overall brain functioning is susceptible to fluctuations in the neurovascular unit [1]. Treatment of the central nervous system (CNS) diseases involves the engagement of the blood-brain-barrier to transport therapeutic agents to impaired brain structures. The BBB has been identified as the highly selective vascular system of the cerebral microvessels composed by a sealed erythrocyte monolayer by tight and adherens junctions precluding molecular paracellular exchange [2,3]. The BBB hinders the transcellular diffusion path, which is confined only to lipid soluble compounds smaller than 400 Da with fewer than nine hydrogen bonds crossing via lipid-mediated transport. To overcome this obstacle current treatment strategies involve transcranial injection or infusion, trans-nasal delivery or employment of medicinal chemistry to chemically alter the nature of the compound so it can cross the BBB through carrier-mediated, receptor-mediated or active efflux transport [4]. However, all of these methods are either invasive, non-targeted and/or involve alteration of the drug composition. The employment of focused ultrasound (FUS) coupled with microbubble administration has been proposed as the only noninvasive technique to transiently, locally and reversibly disrupt the BBB allowing a time and size window for molecules to cross to the brain parenchyma [5,6].

Although the mechanism of BBB disruption with FUS is not entirely clear, it has been proven that the interaction of systemically-injected microbubbles with the capillary walls is the main driving mechanism of the technique. The BBB can be mechanically disrupted by cavitation occurring from the oscillating microbubbles that pass through the focus of the ultrasound beam. This mechanical disruption allows molecules to passively diffuse through the BBB [7,9].

The transition from bench to bedside requires precise selection of parameters that would guarantee targeting accuracy, repeatability and safety. Several studies have been focused on the optimization of the acoustic parameters on various animal models including, mouse, rabbit and non-human primate (NHP) aiming at safe and localized openings [10–17]. While traversing from mouse to NHP, the parameters to be determined in terms of brain complexity and experimental setup increase. Furthermore, the targeting accuracy in NHPs is susceptible to skull aberrations. When sonicating NHPs, the preference of intermediate ultrasound frequencies around 500 kHz solves the tradeoff between irreversible cavitational effects and increased focus at lower frequencies and high phase aberrations and attenuation at higher frequencies [19–22]. It has been reported that increased PNP yields larger openings in a linear trend while shorter pulse lengths and intermediate PRFs are preferred [15,16,19,20]. However, PNP to opening volume correlations in NHP's yielded very low determination coefficients while the cross correlation among animals was inconclusive [19, 21–24]. It has been shown that the normal incidence angle yields larger openings but its relationship with

the opening size and the PNP is yet to be established [25]. The necessity to alter the angle rose from the complexity of the NHP brain and the aim to avoid affecting neighboring areas and vascularized regions. Despite taking into account the angle, however, agreement across animals remains elusive. Therefore, the skull effect was investigated as of affecting the energy propagating to the targeted region. According to the incidence angle of preference, the beam propagates through a varying skull volume resulting in subsequent pressure alterations [25–27]. Moreover, inter-animal skull variation adds to the complexity of the problem.

The study described here aims to provide insight into the uncorrelated results within and among animals by: (i) establishing the relationship between the incidence angle and the BBB opening volume, (ii) employing the skull effect as the correction factor among animals and (iii) evaluating the brain structures' effect on the opening morphology. The first goal was approached by estimation of the angle and its correlation to the BBB opening volume evaluated as the increase in the tissue permeability. Moreover, variation of the applied acoustic pressure offered the opportunity to investigate its effect on the BBB opening volume as the only parameter and in accordance with the angle as well. The skull effect was evaluated at different incidence angles and was utilized as the correction factor to the results. Additionally, the effect of gray and white matter regions on the BBB opening region was assessed by the efficiency of the BBB volume in each structure separately and compared to the corresponding targeted regions. Finally, the selected acoustic parameters fell into the safety window established by previous work of our group and others, verified by the corresponding susceptibility scans reported here [28].

II. Materials and methods

The ultrasound procedure was performed in five male NHPs, i.e. four rhesus macaques (Macaca mulatta) and one marmoset (Callithrix jacchus) (Table I) allowing for a minimum of two-week resting period before subsequent treatment. During each procedure, the animals were immobilized by intramuscular administration of a cocktail containing 1ml ketamine (5–15 mg/kg) and 1ml atropine (5–15 mg/kg) to provide a time window for endotrachial tube placement, catheterization and positioning on the stereotaxic frame. While in the operation room, the animals were anesthetized by inhalation of 1–3% isoflurane. The transducer was attached to the Kopf stereotaxic manipulator to allow for targeting the brain in the stereotaxic coordinate frame, the cornerstone of the targeting analysis. Once the animal was in place and the FUS system was set, a control sonication of 2 seconds was acquired to account as the baseline of the day prior to the sonication with contrast agent administration. The animals were transferred to the MRI site immediately after the sonication (day zero) for assessing the safety of the method and verifying the BBB disruption. Animals tested behaviorally were transferred to the MRI site the day after sonication (day one).

A. Focused ultrasound

The sonications were carried out by a single-element, spherical-segment FUS transducer (H-107, Sonic Concepts, Bothell, WA) operating at 0.5 MHz (radius: 32 mm; geometric

focal length: 62.6 mm, focal length: 34 mm and focal width: 5.85 mm), under the application of a function generator (Agilent, Palo Alto, CA, USA) through a 50-dB power amplifier (E&I, Rochester, NY, USA). A flatband, spherically focused hydrophone (Y-107, Sonic Concepts, WA, USA; sensitivity: 10 kHz to 15 MHz; focal depth: 60 mm, radius 19.75 mm) was confocally mounted at the central void of the transducer to achieve overlap of the two foci. The hydrophone was driven by a pulser–receiver (Olympus, Waltham, MA, USA) connected to a digitizer (Gage Applied Technologies, Lachine, QC, Canada). The acoustic beam profile and the −6 dB focal zone were measured during the calibration process accomplished by the use of a needle hydrophone (HGL-0400, Onda, Sunnyvale, CA, USA). According to previous reports [23,27], the global attenuation due to absorption, reflection and scattering phenomena resulting from the skull thickness was estimated to be equal to 4.92 dB/mm at the center frequency. In-house manufactured, lipid-shell, monodisperse microbubbles with a mean diameter of 4 to 5 μm were diluted to 2×10^5 # bubbles/mL. The microbubbles were intravenously injected through the saphenous vein 10 seconds after the onset of sonication to allow for real-time monitoring of the microbubble cavitation described elsewhere [29]. The animals were sonicated in one or two locations for 120 seconds each, allowing a 20 minute waiting period for microbubbles to be cleared from the circulation, at a pulse repetition frequency of 2 Hz, pulse length of 10 ms and PNP varying from 0.25 MPa to 0.6 MPa.

B. Targeting

Individualized targeting of the ultrasound focus to the brain region of interest was accomplished by employment of a Kopf stereotaxic instrument (Fig. 1). The system provided the user with 9 degrees of freedom; the medio-lateral drive (ML), the stereotaxic arm along the anterior-posterior (AP) direction oriented perpendicularly to the ML drive, the manipulator determining the dorso-vetral (DV) setting oriented perpendicularly to the ML-AP plane, the rotation of the manipulator around the DV-axis (azimuth), the rotation of the manipulator around the ML- or AP- axis (elevation), the selection of right or left stereotactic arm (arm), the relative alignment of the ML- and DV- drives (stereo) and finally the attachment of the transducer to the stereotactic manipulator (finger). In order to predict and evaluate the targeting accuracy, the geometric characteristics of the stereotactic device were analytically implemented into a custom algorithm in MATLAB based on the relative positioning of the nine aforementioned parameters in terms of the stereotaxic coordinate frames. This routine yielded the coordinates of the focal spot and the surrounding ellipsoidal area denoting the focal region in the global coordinate system translated into spatial domain by superposition onto the stereotactically aligned T1-weighted scan accounting for the reference scan for each NHP.

C. Opening verification with MRI

Magnetic resonance imaging was employed to verify the opening and detect potential damage. High-resolution structural T1-weighted sequences (T1 Pre; 3D Spoiled Gradient-Echo, TR/TE = 20/1.4 ms; flip angle: 30°; NEX = 2; spatial resolution: 500 × 500 μm2 ; slice thickness: 1 mm with no interslice gap) were acquired at two time-points for each NHP, before and after BBB opening. The first scan was acquired 30 minutes after IV administration of 0.2 ml/kg contrast agent (gadodiamide) without preceding sonication

accounting as the pre-sonication scan for each NHP while the second scan was acquired after each sonication corresponding to the post-sonication scan. Gadodiamide does not naturally cross the intact BBB because of its molecular size exceeding the threshold (400 Da) and solubility pattern and therefore was utilized as a means of visualizing vessels or structures with increased BBB permeability attributed to hyperintense pixilation. Prior to the sonications, a structural T1-weighted sequence of the same acquisition parameters but spatial resolution of 250 × 250 μm^2 was obtained while the animal was positioned on the stereotactic frame accounting for the reference image. 3D T2-weighted sequence (TR/ TE = 3000/80 ms; flip angle: 90°; NEX = 3; spatial resolution: 400 × 400 μm^2 ; slice thickness: 2 mm with no interslice gap) and 3D Susceptibility-weighted imaging (SWI) (TR/TE = 19/27 ms; flip angle: 15°; NEX = 1; spatial resolution: 400 × 400 μm^2 ; slice thickness: 1 mm with no interslice gap) were utilized to detect edematous and hemorrhagic regions if any [26,30–33].

D. Data analysis

Analysis of the data was performed in two parallel independent processes, the targeting and the imaging analysis, both shown in Fig. 2.

1) Targeting analysis—The targeting pipeline yielded the focal area, the incidence angle and the skull thickness scaling factor. The input values to the algorithm were limited to the nine parameters utilized for the stereotactic configuration at the sonication site and resulted in the vector of axial propagation and the focal area after the application of linear transformations. Fig. 3 illustrates the approach followed for the three-dimensional representation of the BBB opening towards the two dimensional nature of the incidence angle investigated aiming to understand and report its effect on the opening volume. To visualize the targeting on the monkey brain, the resulting ellipsoidal shape was projected on the reference T1-weighted image as shown in Fig. 3a. The information provided by this step was used to estimate the focal area and the center of the focus (Fig. 3b). The next step was the skull extraction from the reference T1-weighted scan by segmentation. The skull line was isolated and mapped onto the global coordinate system by a custom curve fitting algorithm. The superposition of the axial vector on the skull print resulted in their point of intersection I (x_I,y_I,z_I), utilized to obtain the tangent to the skull. The tangent vector was estimated as the derivative of the skull curvature at the point of intersection. The incidence angle was calculated as the angle (α) between the axial vector ($\vec{V}$) and the tangent ($\vec{T}$) as illustrated in Fig. 3c based on their dot product:

$$\alpha = \cos^{-1} \frac{\vec{V} * \vec{T}}{|V| * |T|} \quad (1)$$

The process of incidence angle calculation was repeated at least twenty times for each experiment because of the variance resulting from the tangent vector estimation. The values presented in this paper correspond to the mean incidence angle followed by the variance as the error of the measurement. The analysis was performed in the three-dimensional domain but the angle of interest is being formed by the axial direction (z-direction) described by two

complementary planes, the z-x and the z-y planes. Therefore, the effect of the angle in one of these planes holds for the other as well. The projection of the beam vector onto the skull yielded the thickness to which the corresponding incidence angle was associated. The scaling factor, "sf", was calculated as the ratio of the skull thickness measured at each sonication (d_i) over the maximum measured thickness (d_{max}) to scale the factor to unity.

$$\mathrm{sf}=\frac{d_i}{d_{\max}} \quad (2)$$

Fig. 3d demonstrates two different incidence angles and the resulting variance in the skull thickness facilitating the understanding and the necessity of the concept. Furthermore, the targeting accuracy was evaluated by the Euclidian distance of the BBB opening center O (x_O,y_O,z_O) from the targeting center F (x_F,y_F,z_F). The magnitude of the geometric shift (Δg) is susceptible to the refraction resulting from the variance in the media indices, an estimate of which is given by the corresponding angle shift (Δα) (Fig. 3e).

$$\Delta g=\overline{\mathrm{FO}} \quad (3)$$

$$\Delta a=|\alpha - r| \quad (4)$$

where α stands for the incidence angle and r for the refraction angle.

Finally, the reference scan of each NHP was utilized to construct a five level segmentation map of the monkey brain by employing the K-means segmentation method (Fig. 4). Overlaying the focal area onto the segmentation map revealed the percentage of gray and white matter targeted.

2) Image processing—The image processing algorithm resulted in the volume of opening quantification, the targeting accuracy estimation and the percentage of opened gray-to-white matter ratio. Precise analysis imposed the registration of all T1-weighted images to the reference stereotactically aligned T1-weighted image using FSL's FLIRT routine. According to the sequence fundamentals, bright areas corresponded to increased contrast agent concentration and distribution including vasculature tracts. It is expected though, that in the T1-post images enhancement should also be observed at the BBB disruption site. For each experiment the T1-pre image and the corresponding T1-post image were scaled with the muscle intensity to bring the images in comparable range. Aiming at the extraction of the BBB volume, the ratio of the T1-post over the T1-pre image was obtained, generating the ratio-image. Physiological and magnetic inhomogeneities and asymmetric vasculature resulted in unrelated to opening enhancements that were treated with filtering. Finally, the BBB opening was defined as the integration of the hyperintense voxels exceeding the threshold of 1.1 of the ratio image. The volume of opening presented in this study was normalized by the scaling factor resulting from the targeting algorithm. Embedding the

results obtained from the targeting algorithm to the output of the image processing assured the targeting accuracy of the technique. Specifically, the quantification of the distance between the focal center and the center of mass yielded the axial and lateral shift of the BBB opening from the targeted region. To perform this analysis centroid of the opening was established as the most hyperintense voxel in the surrounding spherical ROI (radius=3mm) of the focal center, assuming linearity between the voxel intensity and the tracer concentration. Fig. 5a shows the BBB opening volume with the coronal contour plot on the back denoting the centers' distance that was further broken down into the shift measured from the three constituent planes: the axial, the sagittal and the coronal. Fig. 5c demonstrates the quantification of the divergence of the opening center from the targeting center. The blue areas correspond to the hyperintense voxels of the BBB opening (>1.1 enhancement of T1 signal) while the red areas are referencing the focal region. The Gaussian shaped ellipsoid (red) is centered at the zero point while the black line denotes the center of the Gaussian-like shape of the activated voxels (blue). The distance of the black line from the zero point defines the shift in that particular dimension while the shift sign in respect to the sonicated side provides insight into the directionality of the opening. For this particular case, the BBB opening center was found 0.25 mm more dorsal, 1.25 mm more medial and 0.75 mm more anterior than the targeted centroid.

The BBB opening center and the tangent plane-to-beam-path intersection define the vector describing the orientation of the BBB opening in space. The angle of this vector with the aforementioned tangent plane was measured as the refraction angle. Finally, superposition of the opening on the segmentation map obtained from the targeting pipeline enabled the quantification of the percentage of the opening laying in gray and white matter.

III. Results

The analysis of 49 sonications resulted in the identification of the correlation between the incidence angle of the axial vector and the BBB opening (V_{BBB}), the estimation of the geometric shift of the V_{BBB} from the target, the skull thickness interference with the incidence angle and finally the V_{BBB} overlap with the underlying physiological structures of white- (WM) and gray matter (GM).

The results presented in the current study correspond to sonications and scans conducted on the same day (day zero) and scans acquired the day after sonication (day one) because of behavioral testing following the sonications [12]. The BBB opening volume decreases over time leading eventually to complete closing and therefore data obtained on day zero and day one are presented separately.

Normalization of the volume of opening with the skull thickness factor enabled BBB opening volume comparisons across animals. In Fig. 6 (a,c) linear regression between the incidence angle, the PNP and the V_{BBB} is illustrated. The determination coefficient is 0.82 for targeting the caudate nucleus (15 cases) and 0.84 for the putamen region (26 cases) on day zero. To facilitate the visualization of the results, bubble charts are provided (Fig. 6 b, d) as the top view of the corresponding scatter plots with the PNP on the horizontal axis, the incidence angle on the vertical axis and the circles correspond to the resulting BBB opening

volume. The radius of the circle increases with the opening volume while in the jet colormap, blue denotes the smallest and red the largest opening. According to Fig. 6(a–d) the V_{BBB} is linearly increasing with the incidence angle and the PNP.

Fig. 6e shows the relationship between the PNP and the volume of opening at a fixed angle. Focusing on the V_{BBB} corresponding to sonications conducted at 76±1.5° and plotting the PNP against the V_{BBB}, a monotonic increase of the opening size with increasing PNP is obtained with a determination coefficient at 0.79. Lower PNP values on the order of 0.3 to 0.35 MPa yield a V_{BBB} equal to 246 mm^3 while sonications at 0.6 MPa induce an opening with a V_{BBB} equal to 854 mm^3. Examples of the BBB opening images for the lowest and highest PNPs applied are demonstrated in Fig. 6f,g. The NHP in Fig. 6f was sonicated at 76±1.5° and 0.35 MPa yielding an opening of 246±22 mm^3 while the NHP in Fig. 6g was sonicated at 76±1.5° and 0.6 MPa yielding an opening of 854±50 mm^3. The figures are contrast-enhanced, T1-weighted images overlaid onto the targeted area as the transparently red colored cylinder and the superimposed opening in jet colormap. These results are in accordance with previous reports of a linear relationship between PNP and BBB opening volume observed in experiments conducted in rodents with a normal incidence angle.

As anticipated, the same trend holds for experiments completed the day after sonication with a decrease in the opening size, because of the gradual closing regime. Fig. 7a,b demonstrates the correlation between the three aforementioned parameters for the Putamen region (23 cases) yielding a determination coefficient equal to 0.90 and indicating a linear increase of the opening size with increasing PNP and incidence angle. The bubble chart provides further insight into the trends observed as the top view of the scatter plot. Fig. 7c illustrates the relationship between the incidence angle and the opening size with fixed PNP. Specifically, a monotonic increase of the V_{BBB} with incidence angle is shown, with a determination coefficient equal to 0.81, for NHPs sonicated at the same PNP (13 cases at 0.4 MPa). Similar results were obtained at other PNPs as well. Incidence angles of 73±1.5° resulted in an opening size of 142±20 mm^3 while close to normal angles, 88±1.2°, yielded opening sizes as large as 481±30 mm^3. Brain images of these cases are provided in Fig. 7d and 7e with the cases presented corresponding to the lowest and highest values of the aforementioned angle range. Both images are contrast-enhanced T1-weighted images overlaid with the targeted area as the transparently red-colored cylinder and the superimposed opening in jet color.

An expected finding observed in Fig. 7a,b is the consistency of V_{BBB} for fixed PNP at 0.3 MPa and incidence angle at 84±0.19° (Fig. 7f). Repeatability of the experiments was achieved by keeping all acoustic and stereotaxic parameters fixed. Brain images of the reproducibility pattern are shown in Fig. 7g and 7h. Both NHPs were sonicated under the same parametric regime and the opening induced was of 440±60 mm^3 for the NHP in Fig. 7g while 451±60 mm^3 for the NHP in Fig. 7h.

Furthermore, to investigate the effect of the underlying brain structures on the opening size, the percentage of gray and white matter at the opening site was estimated and plotted. Fig. 8a demonstrates the percentages targeted while planning the sonication and Fig. 8b illustrates the percentages of the two structures lying at the opening site for each NHP separately. Interestingly, although almost 50% of white matter and 50% of gray matter was

targeted, the induced opening is more restrained in regions of gray matter. The gray-to-white-matter ratio at the opening site is at the order of 80% over 20%.

The targeting accuracy is demonstrated in Fig. 9, whereas the axial shift was 2.36±1.74 mm towards the direction of the transducer while the lateral shift was 1.18±1.05 mm to the lateral direction when targeting the Putamen region (Fig. 9a). For the Caudate nucleus the displacements were 1.58±1.02mm towards the direction of the transducer and 1.05±0.37 mm to the lateral direction (Fig. 9b). The errors correspond to the standard deviations. Apart from the geometric displacement of the opening, its orientation is of equal importance. The angle shift presented in Fig. 9c, d shows that the divergence of the refraction angle from the incidence angle was of 4.5±3° when targeting the Putamen region and 3.65±1.3° at the Caudate nucleus. The displacements and the angle shift for each NHP are presented in Table II analytically.

Finally, Fig. 10 shows representative coronal slices with the rows corresponding to the NHPs and the columns to the T2-weighted and SWI images respectively. These images correspond to the last acquisition for this study and are indicative of any possible damage.

IV. Discussion

The primary goal of the current study is to pave the way for pharmacological agent delivery to targeted neural substrates in primates. Accurate targeting is one of the foremost important aspects while planning the treatment. NHP brains are more inhomogeneous than other animal models and therefore patient-specific procedure is mandatory. Having stressed the significance of targeting, the results presented in this study show the efficacy of the single-element FUS method in targeting specific brain regions, accurately and reliably. However, thorough planning and adjustment of the key components is essential.

Extensive research has been conducted in the opening dependence on various ultrasonic parameters with the PNP being the parameter dictating the opening size. Experiments conducted with a single element transducer operating in mice utilized a normal incidence angle due to the stereotactic geometry. Studies on NHPs refer to the incidence angle as an opening size indicator but do not report any correlation. For this study, extensive research has been conducted to reveal the opening dependence on the angle as a sole parameter as well as in conjunction with PNP.

Fig. 6 and 7 indicate a strong linear correlation between the incidence angle, the PNP and the V_{BBB} independently of the targeted brain structure. The bubble charts reveal the gradual increase of the opening volume in both the direction of increasing PNP and close to normal incidence angle. The bubble chart as a means of visualizing the effect of the parameters utilized to map the volume that corresponds to sets of PNPs and incidence angles.

Pairwise observations provide further insight into the correlations. By keeping the incidence angle fixed and increasing the PNP, the BBB opening volume was steadily increased confirming previous findings in rodents [4]. This observation was confirmed by both qualitative and quantitative results in Fig. 6.

The most interesting finding in this study was the strong dependence of the V_{BBB} on the incidence angle of the propagating wave. Fig. 7 shows that at a fixed PNP, a strong correlation exists between the incidence angle and the V_{BBB}. The pressure applied at most sonications was kept constant and the angle against the opening size was plotted to demonstrate that the opening increases with incidence angle, confirming the hypothesis that a normal angle is preferred for larger openings. This is true due to the shorter propagation path through the skull and thus lower susceptibility to attenuation effects. Finally, the bubble charts show that the color and diameter of the circles change in the pressure direction occur faster in the incidence angle direction. The interpretation of this finding is, as expected, that the opening volume depends primarily on the pressure applied and secondarily on the incidence angle especially at very low or high pressures. However, when sonicating at intermediate pressures, as is usually the case, the incidence angle determines the volume of the opening.

Ultimately, by varying both the PNP and angle, the BBB opening volume can be altered accordingly to achieve the desired treatment by simultaneously protecting the neighboring regions. On the other hand, by keeping both parameters fixed over the course of treatments the same opening can be reproduced. This indicates a priori planning of the incidence angle and the applied pressure for each subject separately.

Another interesting observation is the non-uniform shape of the opening site in several cases, some of which are presented in Fig. 6 and 7. This observation suggests a more thorough investigation of the underlying physiology that could affect the BBB opening volume distribution. Therefore, measurements of the gray- and white matter regions with BBB opening involved in the targeting and opening site were performed. Fig. 8 shows that, regardless of the gray-to-white matter ratio at the targeted and the opened site, the opening percentage on gray matter is in the range of 75–90% while the white matter occupies only 10 to 25% of the opening site. This finding was obtained in all NHPs and was found invariant of the ultrasound parameters. Regional differences in vascularization and subsequent microbubble concentration play a significant role in the probability of inducing an opening. Thorough observation of the brain images of the NHPs reveals discontinuities in the BBB opening volume occurring at the presence of white matter, while other cases show diffusion of the contrast agent in the white matter indicate the need for further studies in the diffusivity mechanism in gray- and white matter.

In terms of accuracy, Fig. 9 suggests that the geometric opening-to-targeting shift was within previously reported and acceptable limits for axial and lateral directions. The overall shift was observed to occur both axially and laterally due to attenuation and refraction phenomena. The unavoidable angle shift due to refraction was estimated to be at 5°.

The NHPs involved in this study were closely monitored to assess the safety of the method. Fig. 10 shows a representative T2-weighted and SWI image for each NHP acquired at the last session. Qualitatively, hyper- and hypo-intense regions were not observed in the respective images establishing the safety of the method. It has to be mentioned that intensity inhomogeneities between the hemispheres could be falsely attributed to damage but thorough visual examination by an expert could eliminate those artifacts. Finally, in terms of

cognition or behavior, no signs of post-procedural clinical deficits in movement, appetite or activity level were noticed. This finding is essential in planning a treatment with multiple sonication sessions in the same region of interest without the risk of a permanent disruption or BBB leakage.

The study presented here has several limitations. The skull extraction algorithm and the fitting process were conducted based on T1-weighted images. As described in the method section, the angle estimation is based on the superposition of the stereotactic geometry on the skull line and therefore the angle calculation could be considered indirect. This indirect method is susceptible to errors resulting from image artifacts, skull extraction algorithm or tangent plane estimation. Averaging eliminates these analysis' errors but a direct method of the angle calculation would be more robust. In order to safely conclude on the exact effect the PNP and the incidence angle have on the opening volume, simulations have to be implemented. Extensive research on varying the incidence angle along the skull line has to be performed in order to create a chart that relates the desired angle with the PNP to achieve an opening of specific volume.

Finally, erroneous positioning of the manipulator and the drivers could result in divergence from the desired and designed focus resulting to misleading interpretations of the results on geometric shift. Further investigation in the white and gray mater diffusion mechanisms is necessary and is pointing towards the direction of diffusion- and perfusion-based MRI.

Further investigation of the diffusion components affecting the physiology of the targeted structures should give more insight into the mechanisms involved in BBB opening.

V. Conclusion

In this study, the dependence of the BBB opening volume on the incidence angle, the effect of the gray-to-white matter ratio on the BBB opening shape and the targeting accuracy were established. It was found that the BBB opening volume increased monotonically with both the incidence angle and PNP. Pairwise observations revealed the linearity between the V_{BBB} and the incidence angle at the same pressure and interchangeably the monotonic increase of the V_{BBB} with PNP at the same angle. As expected, the V_{BBB} induced by the same incidence angle and PNP over the course of several sonications at different days resulted in comparable results. These findings indicate that the BBB opening volume can be predicted and planned by the selection of the corresponding combination of incidence angle and PNP. Additionally, the opening was found to be five times more pronounced in the gray matter than in the white matter indicating the effect of gray-to-white matter ratio on the BBB opened region. Finally the technique was proven accurate and safe given that the shifts were deemed acceptable and that the corresponding safety scans did not show evidence of damage.

Acknowledgments

This work was supported by the National Institute of Health under the Grants RO1- AG038961 and EB009041, the Focused Ultrasound Surgery Foundation and the Wallace H. Coulter Foundation.

The authors thank Amanda Buch (Biomedical Engineering, Columbia University), Carlos Sierra Sanchez (Biomedical Engineering, Columbia University) and Shih Ying Wu (Biomedical Engineering, Columbia University) for their important contribution.

References

1. Abbott NJ, Ronnbac L, Hansson E. Astrocyte-endothelial interactions at the blood–brain barrier. Nat Rev Neurosci. Jan.2006 7:41–53. [PubMed: 16371949]
2. Rubin LL, Staddon JM. The cell biology of the blood-brain barrier. Annu Rev Neurosci. 1999; 22:11–28. [PubMed: 10202530]
3. Pardridge WM. The blood-brain barrier: Bottleneck in brain drug development. NeuroRx: The Journ of the Am Soci for Exp NeuroTher. Jan.2005 2:3–14.
4. Pardridge WM. Drug Targeting to the brain. Pharm Res. Sep.2007 24:1733–44. [PubMed: 17554607]
5. Hynynen K, Mcdannold N, Vykhodtseva N, Jolesz FA. Noninvasive MR imaging-guided focal opening of the blood–brain barrier in rabbits. Radiology. Sep; 2001 220(3):640–646. [PubMed: 11526261]
6. Choi JJ, Pernot M, Brown TR, Small SA, Konofagou EE. Spatio-temporal analysis of molecular delivery through the blood-brain barrier using focused ultrasound. Phys Med Biol. Sep.2007 52:5509–30. [PubMed: 17804879]
7. Sheikov N, Mcdannold N, Vykhodtseva N, Jolesz FA, Hynynen K. Cellular mechanisms of the blood–brain barrier opening induced by ultrasound in presence of microbubbles. Ultrasound Med Biol. Jul.2004 30:979–89. [PubMed: 15313330]
8. Choi JJ, Pernot M, Small SA, Konofagou EE. Noninvasive, transcranial and localized opening of the blood-brain barrier using focused ultrasound in mice. Ultrasound Med Biol. Jan.2007 33:95–104. [PubMed: 17189051]
9. Choi JJ JJ, Wang S, Brown TR, Small SA, Duff KEK, Konofagou EE. Noninvasive and transient blood-brain barrier opening in the hippocampus of Alzheimer's double transgenic mice using focused Ultrasound. Ultrason Imaging. 2008; 30:189–200. [PubMed: 19149463]
10. Treat LH, McDannold N, Vykhodtseva N, Zhang YZ, Tam K, Hynynen K. Targeted delivery of doxorubicin to the rat brain at therapeutic levels using MRI-guided focused ultrasound. Int J Cancer. Aug.2007 121:901–7. [PubMed: 17437269]
11. Mcdannold N, Vykhodtseva N, Hynynen K. Effects of acoustic parameters and ultrasound contrast agent dose on focused-ultrasound induced blood–brain barrier disruption. Ultrasound Med Biol. 2008
12. Choi JJ, Feshitan JA, Baseri B, Wang S, Tung YS, Borden MA, Konofagou EE. Microbubble-size dependence of focused ultrasound-induced blood-brain barrier opening in mice in vivo. IEEE Trans Biomed Eng. Jan.2010 57:145–54. [PubMed: 19846365]
13. Choi JJ, Wang S, Tung YS, Morrison B 3rd, Konofagou EE. Molecules of various pharmacologically-relevant sizes can cross the ultrasound induced blood-brain barrier opening in vivo. Ultrasound Med Biol. Jan.2010 36:58–67. [PubMed: 19900750]
14. Choi JJ, Selert K, Gao Z, Samiotaki G, Baseri B, Konofagou EE. Noninvasive and localized blood-brain barrier disruption using focused ultrasound can be achieved at short pulse lengths and low pulse repetition frequencies. J Cereb Blood Flow Metab. Feb.2011 31:725–37. [PubMed: 20842160]
15. Samiotaki G, Vlachos F, Tung YS, Konofagou EE. A quantitative pressure and microbubble-size dependence study of focused ultrasound-induced blood–brain barrier opening reversibility in vivo using MRI. Magn Reson Med. May; 2011 67(3):769–777. [PubMed: 21858862]
16. Samiotaki G, Konofagou EE. Dependence of the reversibility of focusedultrasound- induced blood-brain barrier opening on pressure and pulse length in vivo. IEEE Trans Ultrason Ferroelectr Freq Control. Nov.2013 60:2257–2265. [PubMed: 24158283]
17. Wang S, Samiotaki G, Olumolade O, Feshitan JA, Konofaqou E. Microbubble type and distribution dependence of focused ultrasound-induced blood-brain barrier opening. Ultrason Med Biol. Jan. 2014 40:130–7.

18. Chen H, Konofagou EE. The size of blood-brain barrier opening induced by focused ultrasound is dictated by the acoustic pressure. J Cereb Blood Flow Metab. Jul.2014 34:1197–204. [PubMed: 24780905]
19. Tung YS, Cho JJ, Baseri B, Konofagou EE. Identifying the inertial cavitation threshold and skull effects in a vessel phantom using focused ultrasound and microbubbles. Ultrasound Med Biol. May.2010 36:840–52. [PubMed: 20420973]
20. Tung YS, Vlachos F, Feshitan JA, Borden MA, Konofagou EE. The mechanism of interaction between focused ultrasound and microbubbles in blood-brain barrier opening in mice. J Acoust Soc Am. Nov.2011 130:3059. [PubMed: 22087933]
21. Marquet F, Tung YS, Vlachos F, Konofagou EE. Feasibility Study of a Clinical Blood-Brain Barrier Opening Ultrasound System. Nano Life. Sep.2010 1:309. [PubMed: 24860623]
22. Marquet F, Tung YS, Teichert T, Ferrera VP, Konofagou EE. Noninvasive, transient and selective blood-brain barrier opening in non-human primates in vivo. PLoS One. 2011; 6:e22598. [PubMed: 21799913]
23. Marquet F, Teichert T, Wu SY, Tung YS, Downs M, Wang S, et al. Real-time, transcranial monitoring of safe blood-brain barrier opening in non-human primates. PLoS One. 2014; 9:e84310. [PubMed: 24505248]
24. Vlachos F, Tung YS, Konofagou EE. Permeability dependence study of the focused ultrasound-induced blood–brain barrier opening at distinct pressures and microbubble diameters using DCE-MRI. Magn Reson Med. Sep.2011 66:821–830. [PubMed: 21465543]
25. Deffieux T, Konofagou EE. Numerical study of a simple transcranial focused ultrasound system applied to blood-brain barrier opening. IEEE Trans Ultrason Ferroelectr Freq Control. Dec.2010 57:2637–2653. [PubMed: 21156360]
26. Arvanitis CD, Livingstone MS, Vykhodtseva N, McDannold N. Controlled ultrasound induced blood brain barrier disruption using passive acoustic emissions monitoring. PLoS One. 2012; 7:e45783. [PubMed: 23029240]
27. Wu SY, Tung YS, Marquet F, Downs ME, Sierra Sánchez CJ, Chen CC, et al. Transcranial cavitation detection in primates during blood-brain barrier opening—a performance assessnebt study. IEEE Trans on Ultrason Ferroelectr Freq Control. Jun.2014 61:966–978.
28. Hynynen K, McDannold N, Sheikov NA, Jolesz FA, Vykhodtseva N. Local and reversible blood–brain barrier disruption by noninvasive focused ultrasound at frequencies suitable for transskull sonications. Neuroimage. Jan.2005 24:12–20. [PubMed: 15588592]
29. Feshitan JA, Chen CC, Kwan JJ, Borden MA. Microbubble size isolation by differential Centrifugation. Journ Colloid Interface Sci. Jan.2009 329:316–24.
30. Kinoshita M, McDannold N, Jolesz FA, Hynynen K. Targeted delivery of antibodies through the blood–brain barrier by MRIguided focused ultrasound. Biochem Biophys Res Commun. Feb.2006 340:1085–90. [PubMed: 16403441]
31. Yang FY, Fu MW, Yang RS, Liou HC, Kang KH, Lin WL. Quantitative evaluation of focused ultrasound with a contrast agent on blood-brain barrier disruption. Ultrasound Med Biol. Sep.2007 33:1421–7. [PubMed: 17561334]
32. Liu H, Wai Y, Chen W, Chen J, Hsu P, Wu X, et al. Hemorrhage detection during focused-ultrasound induced blood-brain-barrier opening by using susceptibility-weighted magnetic resonance imaging. Ultrasound Med Biol. Apr.2008 34:598–606. [PubMed: 18313204]
33. Yang FY, Liu SH, Ho FM, Chang CH. Effect of ultrasound contrast agent dose on the duration of focused-ultrasound-induced blood-brain barrier disruption. J Acoust Son Am. Dec.2009 126:3344–9.
34. Downs ME, Buch AM, Karakatsani ME, Sanchez Sierra C, Konofagou EE, Ferrera VP. Long-Term Safety of Repeated Blood-Brain Barrier Opening via Focused Ultrasound with Microbubbles in Non-Human Primates Performing a Cognitive Task. PLoS One. 2015; 10:e0125911. [PubMed: 25945493]

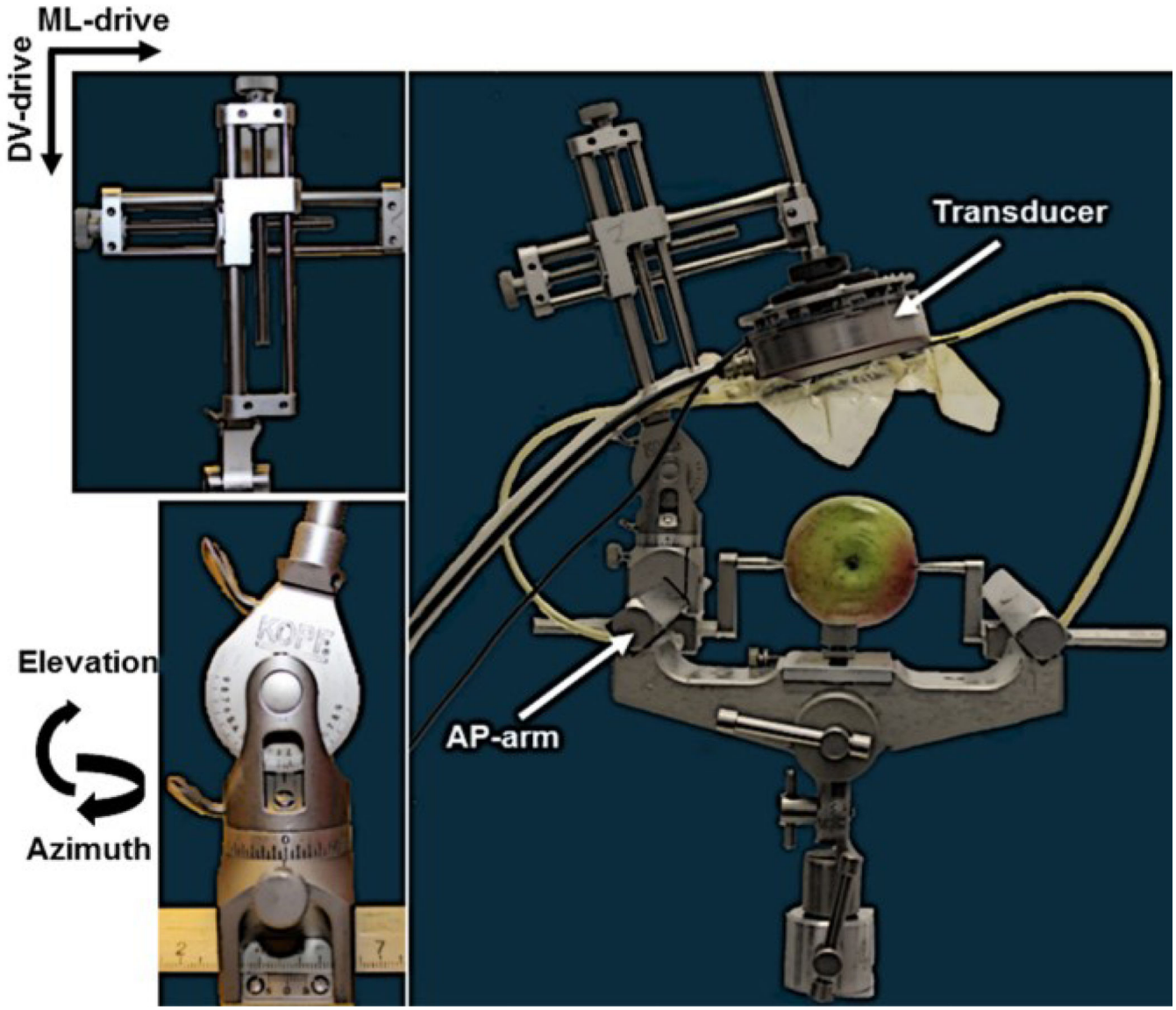

Fig. 1.
Experimental setup and stereotactic frame.

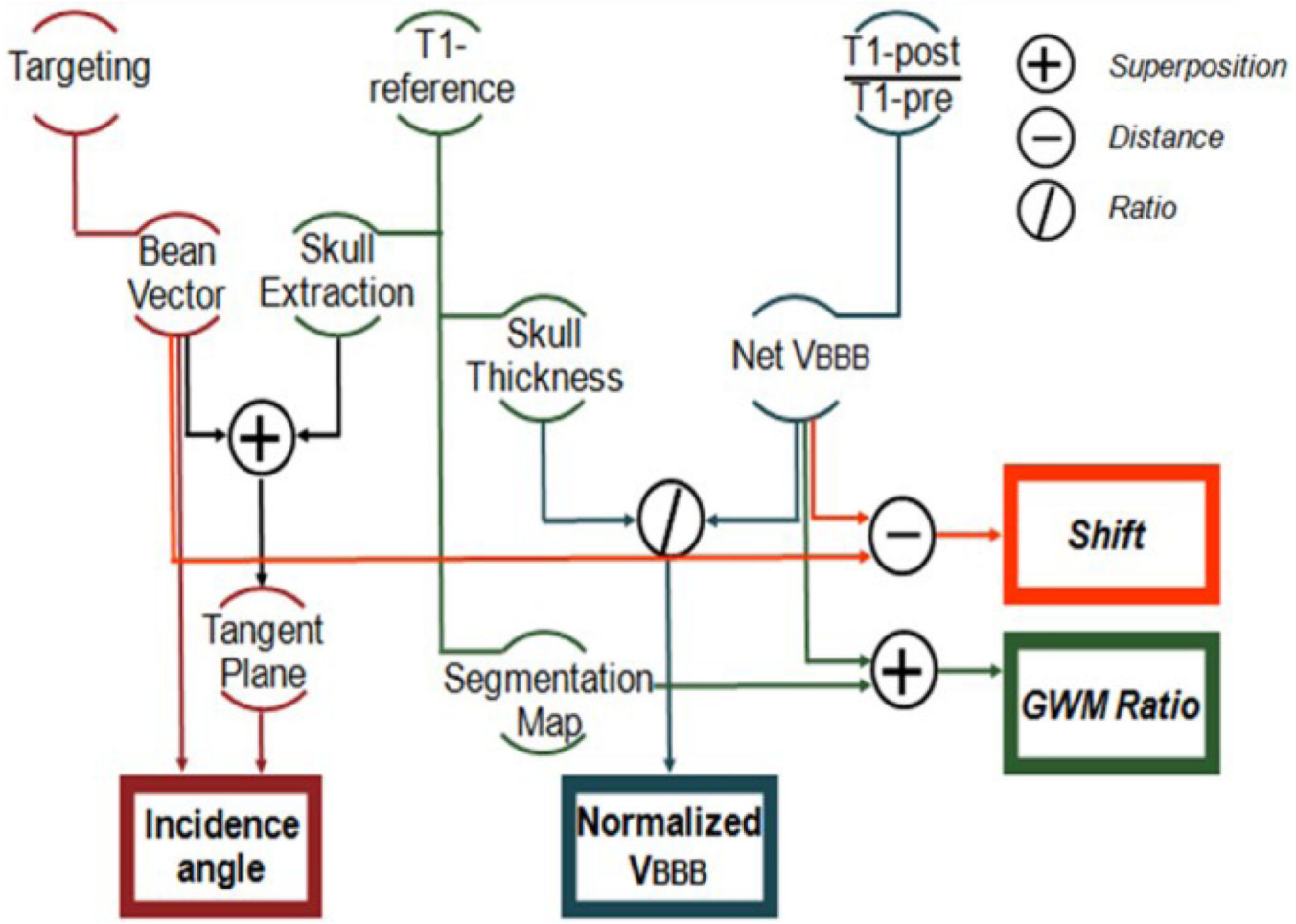

Fig. 2.
Flow chart of the data analysis.

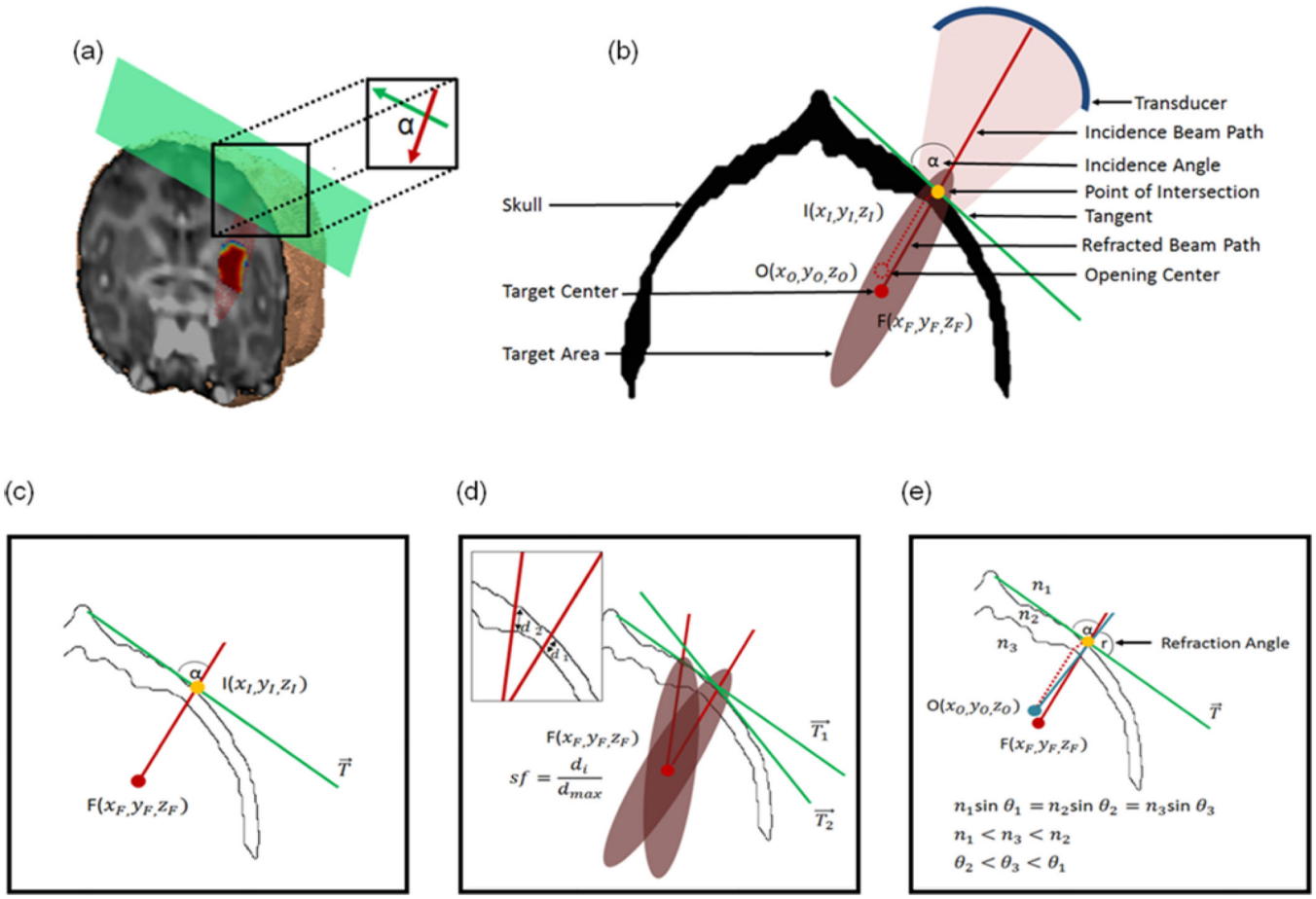

Fig. 3.

(a) 3D reconstruction of the BBB opening with the focal region of the axial vector (red cylinder), the tangent plane on the skull (green plane) and the incidence angle (α) projected. (b) Schematic of the skull and definitions of the abbreviations used. (c) Closer look at the schematic to define the incidence angle. (d) Closer look at the schematic to define the skull thickness factor, sf, for two different incidence angles. (e) Closer look at the schematic to define the refraction angle.

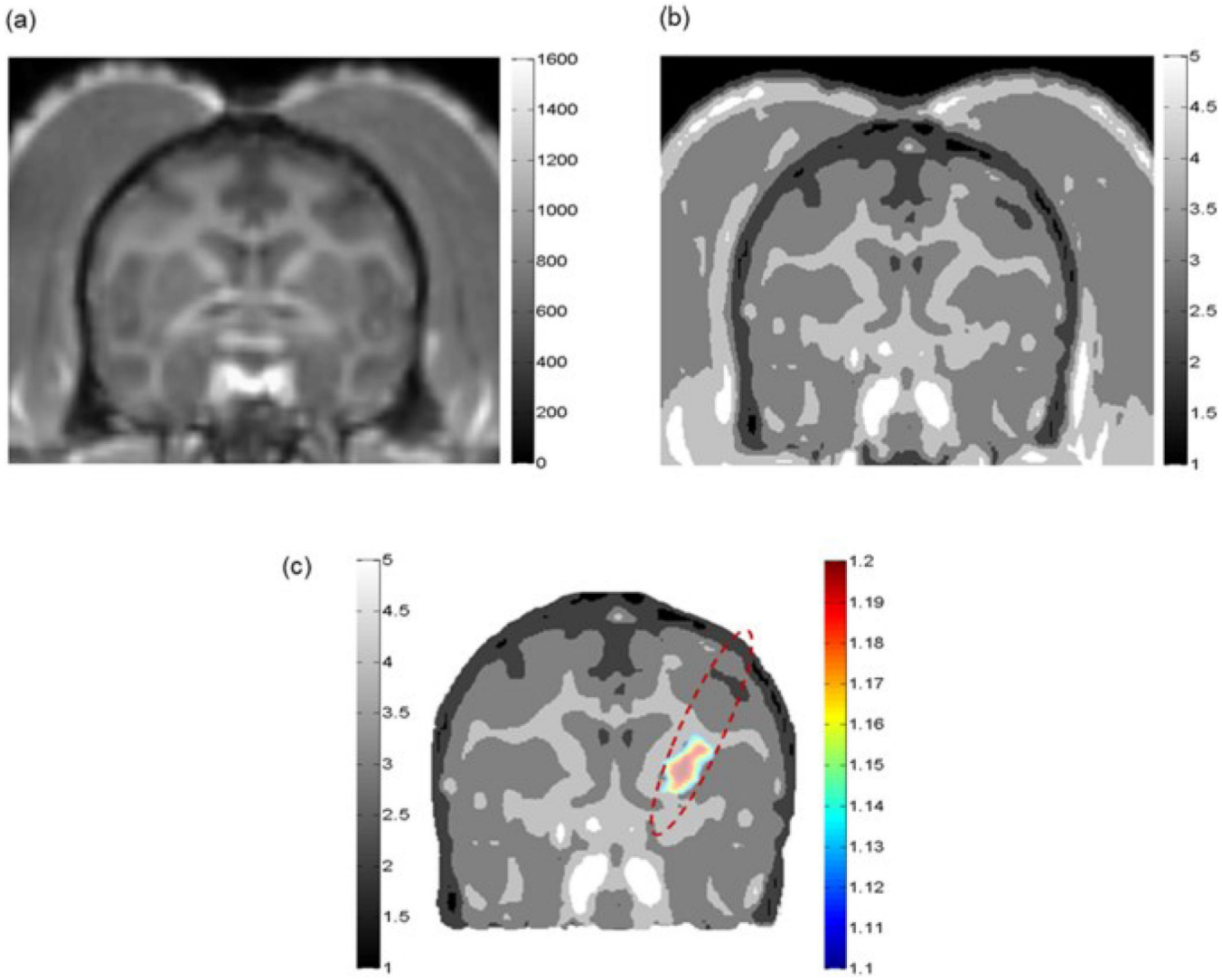

Fig. 4.

Estimation of the Gray-to-White-Matter ratio on a segmented brain T1 weighted image. (a) T1 weighted image. (b) Segmentation of the image. (c) Overlay of the BBB opening on the segmented image with the focal area delineated by the dotted red line.

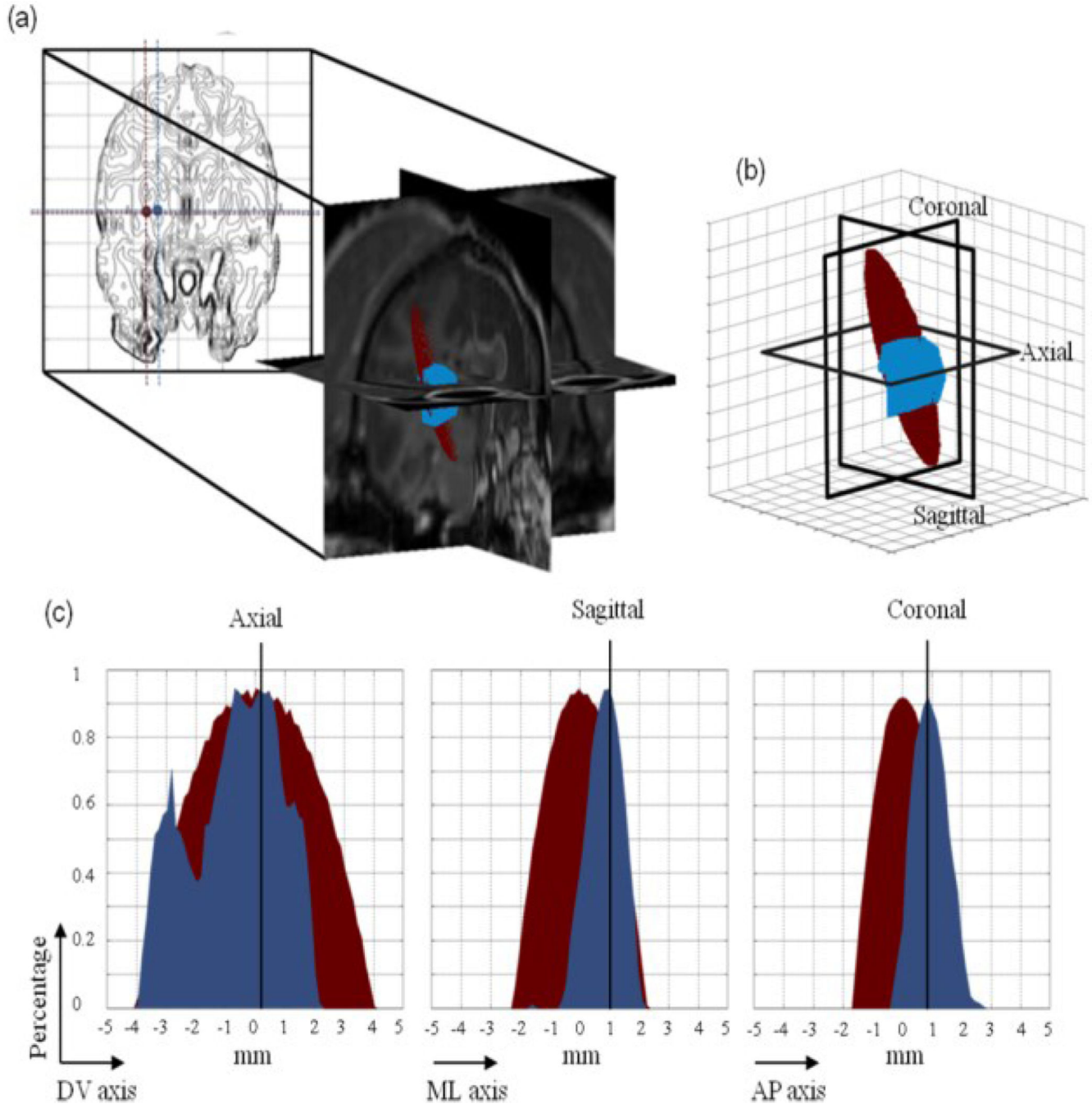

Fig. 5.

Calculation of the shift between the actual opening center (blue) and the targeted center (red). (a) 3D representation of the ellipsoid denoting the focal area and the BBB opening volume projected on the three planar views. The contour plot of the coronal plane is utilized to visualize the distance between the two centers. (b) 3D representation of the BBB opening and the targeted area. The three planes are also denoted. (c) The three panels correspond to the opening-to-targeting shift measurement over the three directions, DV, ML, AP. The blue areas correspond to the hyperintense voxels of the BBB opening (>1.1% enhancement of T1

signal) while the red areas are referencing the focal region. The Gaussian shaped ellipsoid (red) is centered at the zero point while the black line denotes the center of the Gaussian-like shape of the activated voxels (blue). The distance of the black line from the zero point defines the shift in that particular dimension while the shift sign in respect to the sonicated side provides insight into the directionality of the opening. For this particular case the opening center was found 0.25 mm more dorsal, 1.25 mm more medial and 0.75 mm more anterior than the targeted center.

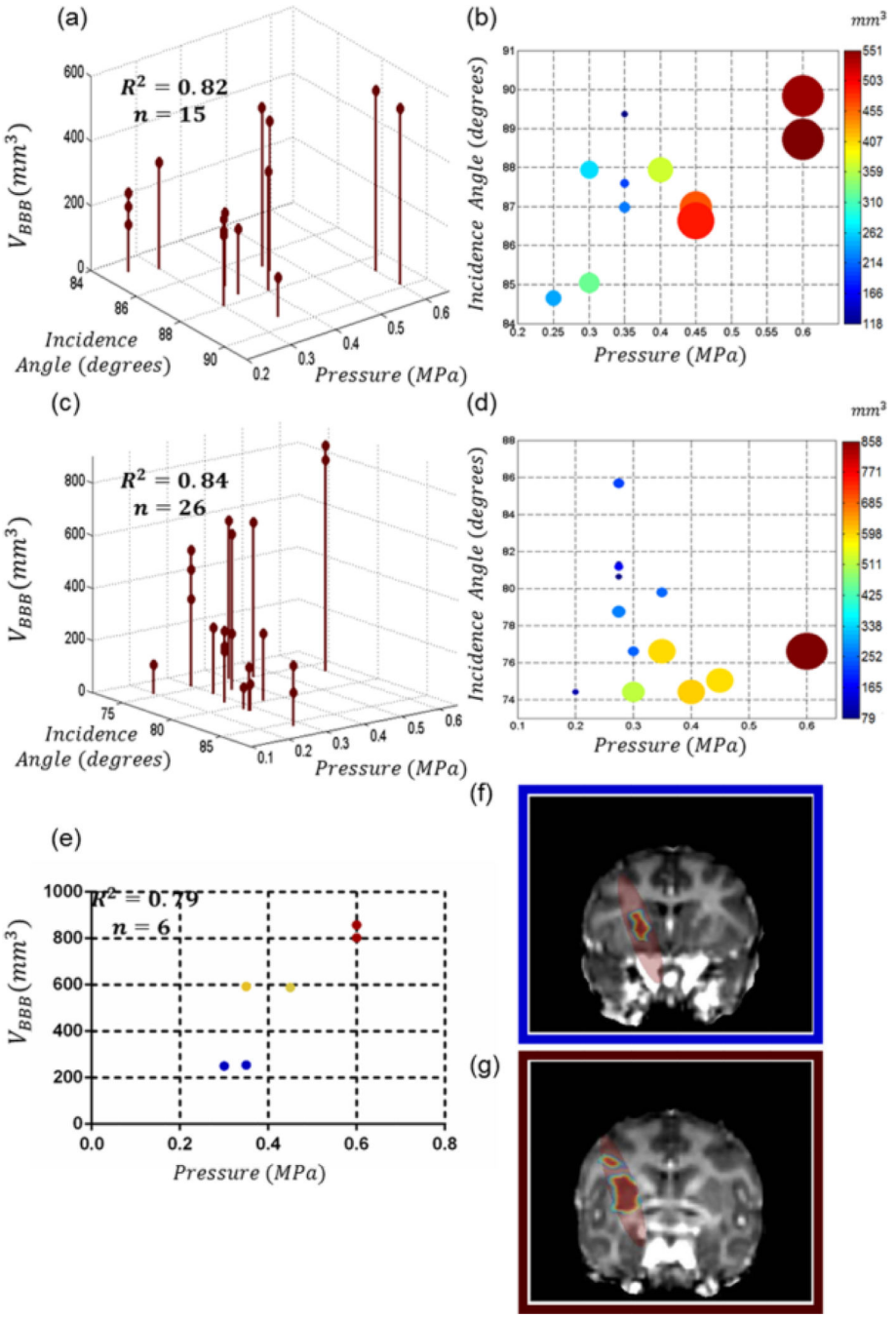

Fig. 6.

(a–d): Linear fitting of the incidence angle, the pressure and the normalized volume of opening. The results correspond to findings on the day of sonication at the (a,b) caudate nucleus and (c,d) putamen region. The panels on the left side demonstrate the fitting in the three dimensions while the panels on the right side are two dimensional volume maps. The pressure and the incidence angle correspond to the horizontal and vertical axis respectively while the volume of opening is shown as the intensity at the cross-sections. The colorbar provides numerical information regarding the opening volume. (e) Linear fitting of the

pressure and the normalized volume of opening at the angle of 76±1.5°. The results correspond to findings on day zero at the putamen region. (f,g): Brain images showing linear increase of the volume of opening with increasing pressure for fixed incidence angle. (f) Sonication at 76±1.5° and 0.35 MPa yielded an opening of 246±22 mm^3 (g) Sonication at 76±1.5° and 0.6 MPa yielded an opening of 854±50 mm^3

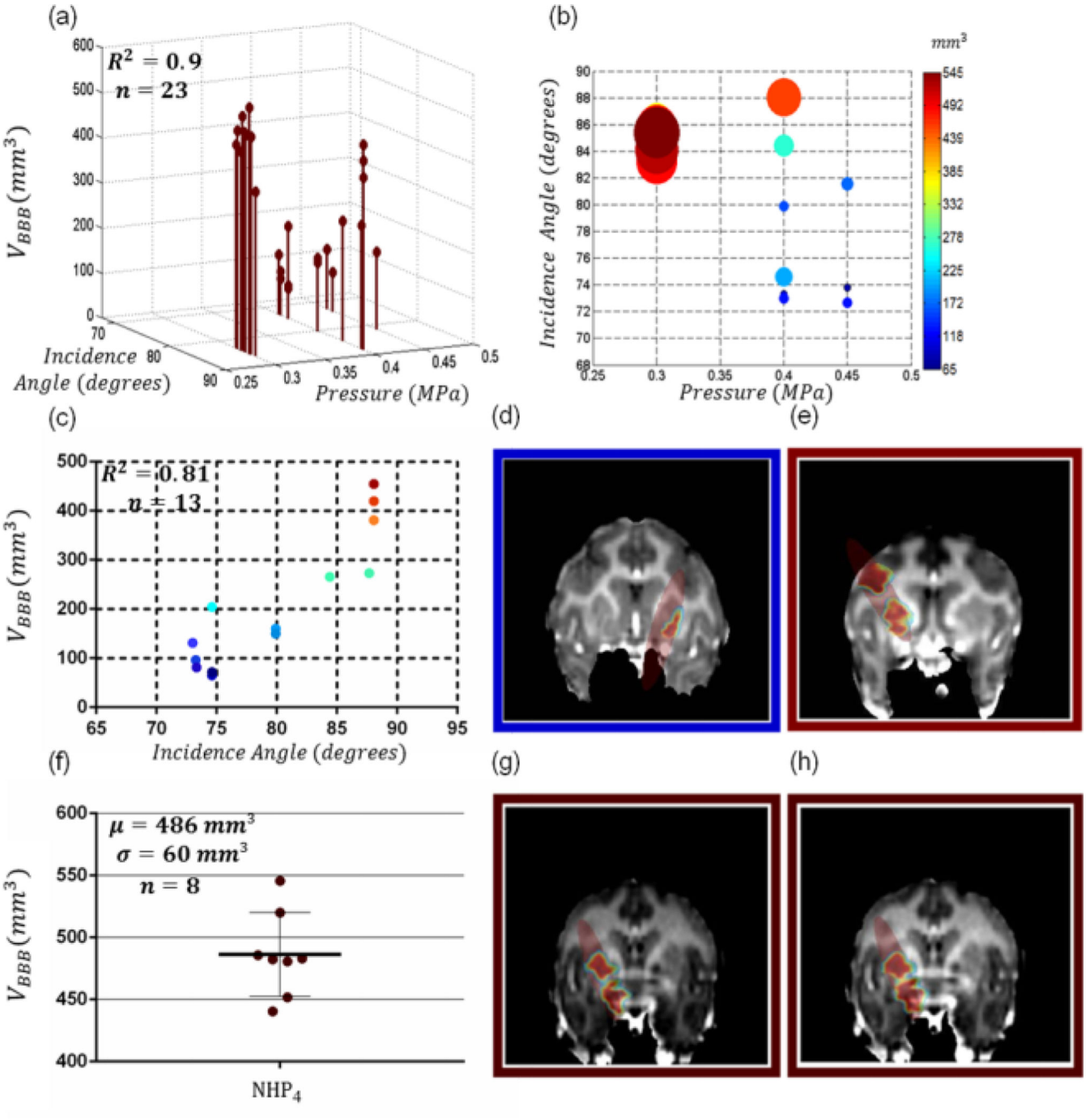

Fig. 7.

(a,b): Linear fitting of the incidence angle, the pressure and the normalized volume of opening. The results correspond to findings on day one at the putamen region. (a) The panel demonstrates the fitting in the three dimensions while (b) the panel on the right side is a two dimensional volume map. The pressure and the incidence angle correspond to the x- and y-axis respectively while the volume of opening is shown as the intensity at the cross-sections. The colorbar provides numerical information regarding the opening volume. (c) Linear fitting of the incidence angle and the normalized volume of opening at 0.4 MPa. (d,e):

Qualitative results showing linear increase of the volume of opening with increasing pressure for fixed incidence angle. (d) Sonication at 73±1.5° and 0.4 MPa yielded an opening of 142±20 mm^3 (e) Sonication at 88±1.2° and 0.4 MPa yielded an opening of 481±30 mm^3 (f) The graph is demonstrating the mean and standard deviation values for eight experiments conducted on the same animal under the same parameters. (g) Sonication at 84±0.19° and 0.3 MPa yielded an opening of 451±60 mm^3 (h) Sonication at 84±0.19° and 0.3 MPa yielded an opening of 440±60 mm^3 when sonicated again.

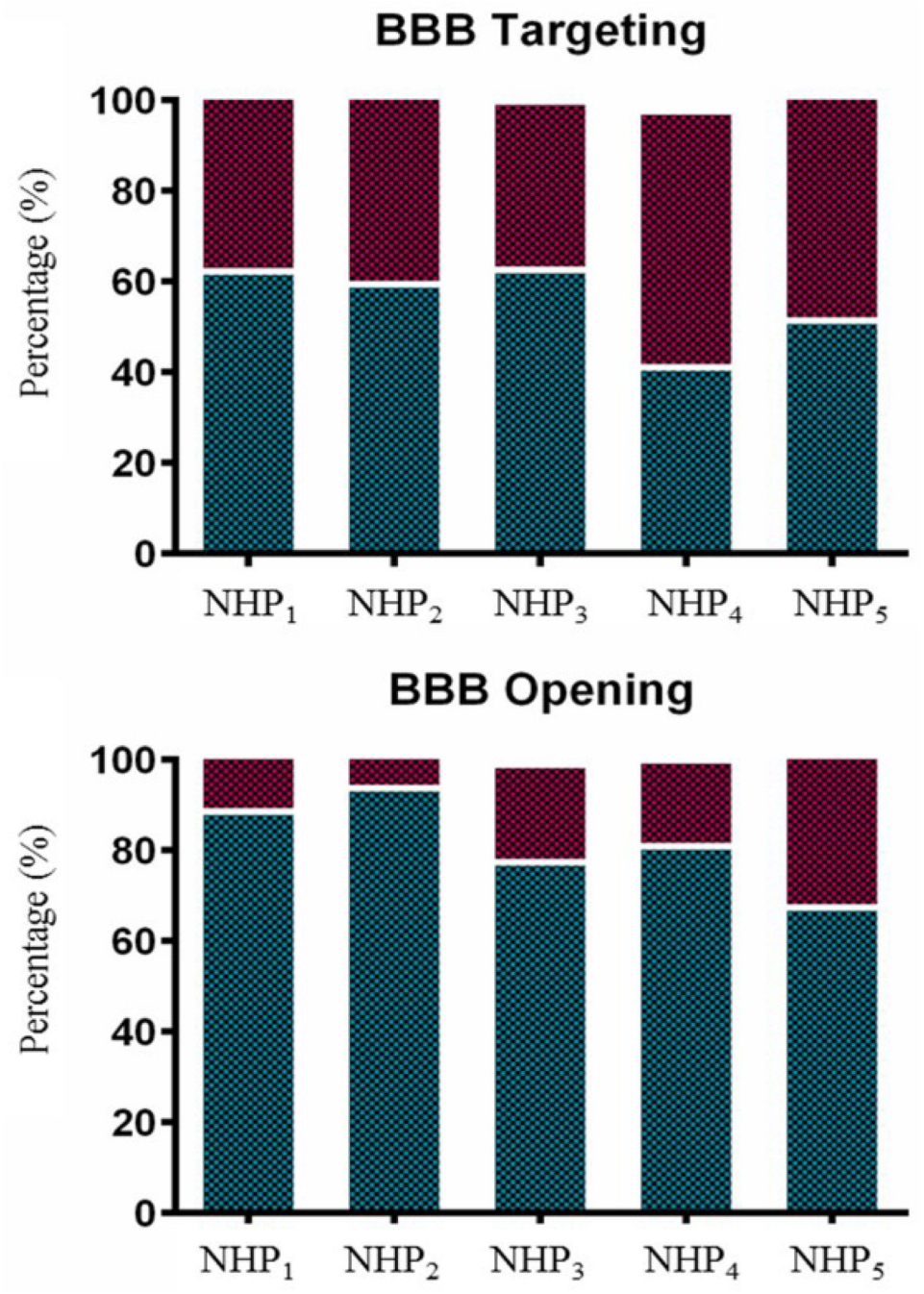

Fig. 8.
Gray-to-White-Matter ratio at the (a) targeted area and (b) the opening site.

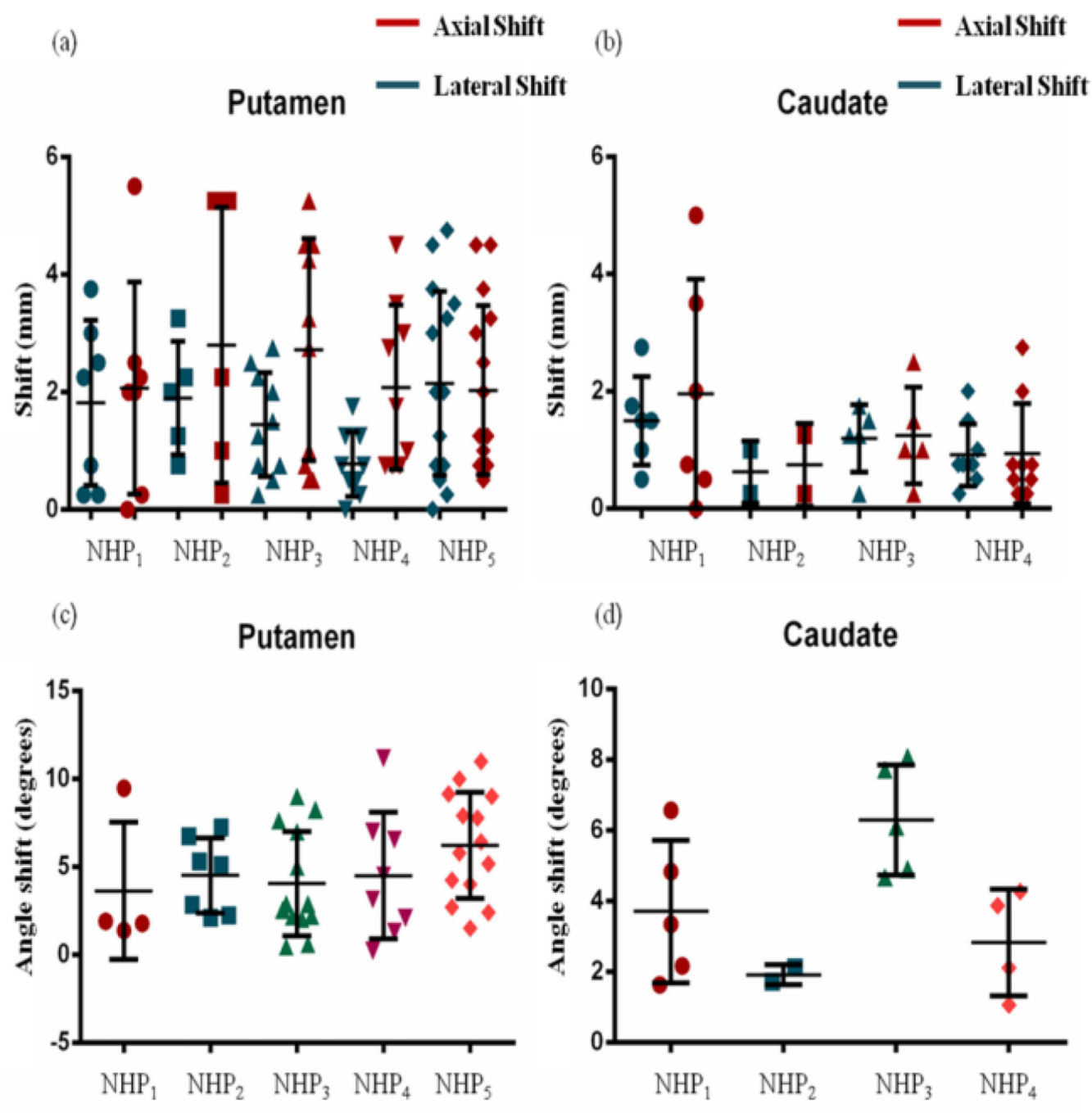

Fig. 9.

(a) – (b) The axial and lateral shift between the opening center and the targeted focus for each NHP at the putamen region and the caudate nucleus respectively. (c) – (d) The angle shift for each NHP obtained as the difference between the incidence and refraction angle at the putamen region and the caudate nucleus respectively.

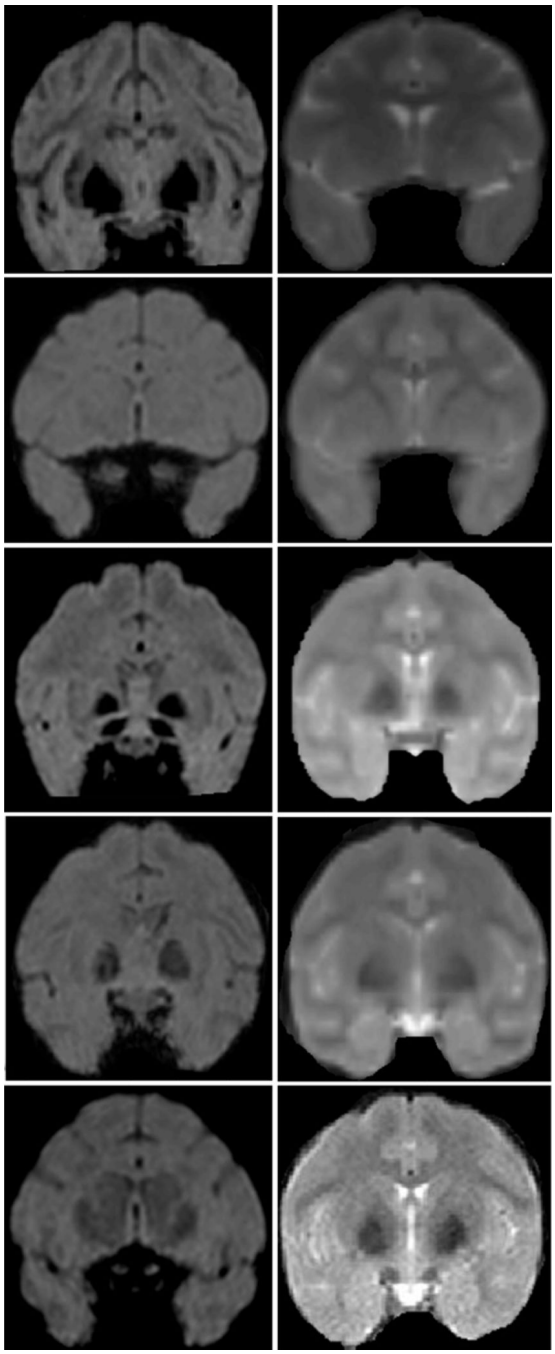

Fig. 10.
SWI (left column) and T2 weighted (right column) scans were performed to assess the safety of the method. Each row corresponds to an NHP.

Table I

Non-Humane Primate characteristics.

	Species	Age (yrs)	Weight (kg)	Number of sonications	
				Putamen	Caudate
NHP$_1$	Rhesus Macaques (Macaca mulatta),	21	10	8	6
NHP$_2$	Rhesus Macaques (Macaca mulatta)	21	9	7	2
NHP$_3$	Rhesus Macaques (Macaca mulatta)	20	10	10	5
NHP$_4$	Rhesus Macaques (Macaca mulatta)	10	9	15	4
NHP$_5$	Marmoset (Callithrix jacchus)	14	6	9	-

Table II

Geometric and angle shifts of each NHP per region.

	Axial Shift		Lateral Shift		Angle Shift	
Region	**Putamen**	**Caudate**	**Putamen**	**Caudate**	**Putamen**	**Caudate**
NHP_1	2±1.8	1.9±1.9	1.8±1.4	1.5±0.7	3.6±3.8°	3.7±2°
NHP_2	2.8±2.3	0.75±0.7	1.9±0.9	0.6±0.5	4.5±2.1°	1.9±0.2°
NHP_3	2.7±1.8	1.2±0.8	1.4±0.8	1.2±0.5	4±2.9°	6.2±1.5
NHP_4	2±1.4	0.9±0.8	0.7±0.5	0.9±0.5	4.5±3.6°	2.8±1.5°
NHP_5	2.3±1.4	-	2.1±1.5	-	6±3°	